A Study on Error Propagation in DEM Analysis and Its Impact on Correction of Remote Sensing Data

Pei-Chun CHANG

Master's Program in Environmental Sciences, University of Tsukuba

1. Introduction

1.1 Objective

The objective of this study is to evaluate how errors in the digital elevation model (DEM) propagate into the derivative product, namely the cosine map of solar incident angle, from geographical information system (GIS) operations and its impact on the satellite derived surface reflectance. The Monte Carlo method (MCM) of simulation for error propagation was employed for quantifying the errors of satellite derived surface reflectance contributed by DEM errors.

In this study, Yakushima, which is an island located at southern Japan, was selected as the test site. A spatial autocorrelation random filed served as the error field was generated and added to the grid-based DEM. The degree of the spatial autocorrelation of the DEM errors was estimated from the standard deviation of the DEMs generated from the vector contour line data. Then the realized DEM was used for the atmospheric and topographic corrections of the Landsat TM 5 data. By repeating the procedures described above and taking their mean and standard deviation, the magnitude and spatial distribution of the errors of the surface reflectance contributed by the DEM errors were estimated.

1.2 Background

For the geographical data stored in the GIS, they may, at least to some extent, be contaminated by errors. When geographical data are the input to some GIS operation, as a result, the output may not be sufficiently reliable for making correct conclusions since the input data are not error-free. The error within the input may therefore contribute to the error in the result of a GIS operation.

For the grid-based DEM, the overall errors can be regarded as the combination of errors in the contour map itself, from which a DEM was produced, the errors arising from digitizing and the interpolation error. Instead of providing a map form of errors for each DEM (i.e., the spatial distribution of the DEM errors), the producer of the DEM usually provides the magnitude of errors in a summarized form, the root mean square error (RMSE) of the DEM, for accuracy assessment. For example, USGS's 7.5-minute level 1 DEM has a vertical RMSE of seven meters in general and up to a maximum of 15 meters (USGS, 1998). RMSE is expressed as:

$$\mathrm{RMSE} = \left[\frac{1}{n}\sum (z - z^*)^2\right]^{0.5} \qquad (1)$$

where n = the number of test points, z = the elevation of the DEM at test point and z^* = the true elevation at test point measured by higher precision equipment. A minimum of 28 test points per DEM is used to compute the RMSE, which is composed of a single test using 20 interior points and 8 edge points (USGS, 1998). It is usually assumed that the error of a grid point in the DEM is normally distributed with

the zero mean and the standard deviation equals to the RMSE (Hunter and Goodchild, 1997). Calculations of surface parameters from the DEM such as slope gradient and aspect usually involve the neighborhood operation, that is, the new attribute value at a grid point is derived from the elevation at the same point in combination with elevations of the surrounding grid points. This further complicates the problem and hence the errors within the DEM can not be treated independently. Through the error propagation approach, the problem described can be addressed. The results of error propagation analyses come with confidence intervals or other measures of reliability, providing a more realistic depiction of the effects of data uncertainty on the application question.

Evaluation of the error propagation effect on the results of GIS analyses can be divided into two categories. In some cases, especially the point operation (i.e., the output of a GIS operation for an entity or a grid point only relates to the input for the same entity or grid point), it is possible to evaluate error propagation analytically by the classical error analysis theory. In an analytical approach, the error of an output through a GIS operation can be modelled by taking the first or second derivative of the GIS operation by Taylor series expansion (Heuvelink, 1998, pp. 36-39).

Another approach is to adopt the Monte Carlo method (MCM). An error term, usually drawn from the Gaussian probability distribution function, is added to the input variable and GIS operation is then carried out to obtain a realization of output. Many realizations are generated for representing the entire population of outputs. The outputs are then aggregated for the calculations of the mean and the standard deviation, which represent the estimate and error of the output respectively. (Heuvelink, 1998, pp. 40). Although the MCM approach requires much more computational intensity than the analytical approach, it has several important advantages: 1) it can yield the entire distribution of the output of the GIS operation at any level of precision; 2) it can be applied to any kind of the GIS operation regardless of complexity; and 3) spatial autocorrelation of errors can be taken into account.

2. Study Area

The test area for this study is Yakushima, a circular island located at 30°30' N and 130°28' E, 135 km south of Kagoshima City, Japan (Figure 1). The island is some 24 km long from north to south and 28 km wide from east to west at the widest point. The coastline, which is about 132 km long, encompasses an area of 503 km^2. The reasons for selecting Yakushima as a test site are: 1) the availability of the vector contour line data, and 2) the varieties of landform, including flat surfaces in the coastal areas and rugged terrains in the inland mountainous areas.

3. Data

DEM data

The DEMs used in this study are the 50 m DEM of Digital Map series dataset published by the Geographical Survey Institute of Japan (GSI). The DEMs were produced from vector contour lines data through interpolation to equal-spaced grids. The coordinate system is the geographic coordinate system (latitude/longitude) with the Bessel ellipsoid and the Tokyo datum. The grid spacing is about 2.25" of longitude and 1.5" of latitude, which is approximately 50 m. The

RMSE of the DEM is about 7.2 m on the ground (Murakami, 1995).

Vector contour data

With the permission of the GSI, it was able to use the dataset of the vector contour lines (Arcview shapefile format) that was used to produce the GSI's 50 m DEM. The source data of the vector contour lines are the contour lines of the GSI's 1:25,000 Topographic Map Series. Contour lines were first scanned and rasterized with a resolution of 50 µm and then transformed to vector contour lines. The purpose to use this dataset is to estimate the spatial structure of errors in the GSI's 50 m DEM.

Satellite data

The satellite data used in this study is a Landsat 5 TM image acquired on 05 March 1993 (scene ID L5TM19930305D112039). The major reasons for selecting this image for the study were: 1) the cloud coverage of the whole scene was about 11-20% with almost no cloud over the island and hence performing atmospheric correction was much easier; and 2) vicarious radiometric calibration coefficients were available to reduce the uncertainties caused by the degradation of the sensors's sensitivities.

4. Procedures of Analysis

4.1 Introduction

Before the Monte Carlo method was applied to simulate the error propagation, the DEM and satellite data were preprocessed. The preprocessings include: (1) reprojection and resampling of the DEM and satellite data; (2) conversion of digital number to at-satellite reflectance of the satellite data; (3) estimation of the spatial autocorrelation of the DEM error by utilizing vector contour line data with geostatistics method; and (4) estimation of the atmospheric correction parameters using the 6S code. After all these preprocessings were done, the data were used to the MCM simulation. A single MCM simulation includes: (1) generation of the spatial autocorrelative DEM error field and the error perturbed DEM; (2) generation of a map of the cosine of solar incident angle; and (3) atmospheric and topographic corrections of the satellite data. The simulation was repeated up to 300 times, and the means and the standard deviations of these simulation results were calculated. The total work flow of this study is summarized in Figure 2.

4.2 Calculation of cosine of solar incident angle from the DEM

The rationale of the physically-based topographic correction to the satellite image is to adjust the amount of direct solar irradiance at the tilted surface. This can be done by calculating the cosine of solar incident angle. The cosine of solar incident angle of the ground can be calculated from the slope gradient and aspect derived from the DEM, and the solar zenith and azimuth angles provided by satellite data. The DEM slope gradient and aspect were calculated using the Horn's method (Horn, 1981). This method was reported to be better among other methods for calculating slope gradient and aspect from the DEM (Jones, 1998). Since the original 50 m DEM is georeferenced to the geographical coordinate system, the first step was to reproject the DEM to the universal transverse mercator (UTM) coordinate system with Bessel ellipsoid and Tokyo datum. To match the spatial resolution of the TM image, which is 30 m except for the band TM6, the 50 m DEM was resampled to 30 m using the bilinear interpolation method. It is assumed that

the elevation accuracy remains at 7.2 m after the reprojection and resampling.

4.3 Estimation of spatial autocorrelation of errors in DEM and error field generations

As previous studies have showed that the spatial structure of DEM errors greatly affects the results of the GIS operations (Hunter and Goodchild, 1997), the spatial autocorrelation of the DEM errors must be taken into account. In ideal situation, an error map of the DEM would be simulated using conditional simulations with the error structure modeled using spot heights, which may be obtained either from the DEM with higher accuracy or field surveys. Each simulation is conditioned by not only the error structure but also the known elevation errors (i.e., DEM errors at the locations where higher accuracy data are available remain unchanged) and thus most realistic error fields can be generated.

Unfortunately, this is not always the case. DEMs with higher elevation accuracy are not always available, especially in developing countries. Furthermore, geostatistical tools used to measure the spatial autocorrelation usually require at least 50-100 data points for a stable result. This also increases the difficulty for field measurements if the target area is large.

To overcome this problem, an alternative approach was employed to estimate the spatial autocorrelation of the DEM errors. In the first stage, a series of DEMs with the spatial resolution of 30 m were generated from the GSI vector contour line data. The interpolation algorithms used to generate a DEM included inverse distance weight, radial basis functions, global polynomial method, local polynomial method, ordinary kriging, and triangular irregular network to grid conversion. By changing the parameters for interpolation, 14 different versions of the DEMs were generated. Then the standard deviation of the generated elevations at each grid point was calculated and the result shown in Figure 3. Since there were no field measurements available, it was impossible to know where the elevations of the DEM were higher or lower than the actual elevations.

By generating the standard deviation of each grid point of the DEMs, it was assumed that the possible error structure of the DEM can be estimated from this information using a geostatistics method. One point should be addressed is that the approach adopted here only aims to model the spatial autocorrelation of the elevation errors. The magnitude of the elevation errors is modelled using the RMSE of the GSI · 50 m DEM, which is an estimate for the whole DEM dataset covering Japan. However, using the RMSE of the DEM for error modelling might underestimate the elevation errors in rugged terrains and overestimate in flat areas. As shown in Figure 4, the standard deviation of the generated DEM is larger in high slope gradient areas than in low slope gradient areas, so higher possibility of large DEM errors will occur in rugged terrains than in at areas. Thus using the theoretical RMSE of the DEM can be regarded as a tradeoff if the real DEM errors are unknown. Then the spatial structure of the elevation errors is determined by calculating the semivariance of the standard deviation of each grid point of the DEMs. The semivariance $\gamma(h)$, which is used for describing the degree of spatial autocorrelation, is defined as (Burrough and McDonnell, 1998, pp. 134):

$$\gamma(h)=\frac{1}{2n}\sum_{i=1}^{n}[z(x_i)-z(x_i+h)]^2 \qquad (2)$$

where $[z(x_i), z(x_i+h)]$ are the standard deviations of elevation at grid points $[x_i, x_i+h]$ separated by a distance lag h. When the semivariance is plotted against distance lag h, the resulting graph is known as semivariogram or simply variogram. Semivariogram provides a mean for: (1) identifying spatial patterns; (2) optimal interpolation from sample data; and (3) determining an optimal sampling scheme. Since the histogram of the standard deviation was highly positively skewed and many geostatistics methods assumed the normal distribution, it was transformed using natural logarithms before computing the experimental variogram. The experimental variogram and its fitted model are shown in Figure 5.

Sometimes the spatial variation along certain direction is more continuous than along others. Hence, the spatial autocorrelation changes not only with the distance but also with the direction between two locations. This is called the anisotropy. There are two types of anisotropies: geometric anisotropy and zonal anisotropy. Geometric anisotropy refers to the variation of the range of the variogram with respect to the orientation while zonal anisotropy refers to the variation of the sill of the variogram with respect to the orientation (Stein et al., 1999, pp. 70). By specifying a search direction and the angle of tolerance, the experimental variogram for certain direction can be calculated. Diagrams for directional variograms showing geometric anisotropy and zonal anisotropy and fitted models are shown in Figure 6 and Figure 7, respectively.

To fit the geometric anisotropic variogram in two-dimensional case, the range parameter can be defined as an ellipse with the orientation of the maximum range (direction of spatial autocorrelation at the longest distances), the minimum range (range perpendicular to the maximum range), and an anisotropy ratio, which is the ratio of the minimum range to the maximum range. Eriksson and Siska (2000) showed that the zonal anisotropy can be modelled using the same procedure used to model the range anisotropy.

After determining the spatial structure of the DEM errors, this information together with the DEM RMSE was used to generate a spatial autocorrelative error field using unconditional gaussian simulation. Unconditional gaussian simulation is a method that can be used to generate normally-distributed realizations with prescribed statistics (e.g., mean, variance and variogram) without incorporating any observation data. This means that the realization of the unconditional gaussian simulation honors the form of the spatial structure (variogram models) that was used to generate it, but the realization is not forced to pass through any particular attribute at any particular location. Figure 8 shows a realization having the zero mean and variograms of the standard deviation of each grid point of the DEMs. The standard deviation of the realization was set to 7.2 to match with the RMSE of the GSI's 50 m DEM.

4.4 Atmospheric and topographic corrections of the satellite data

Under the assumption of horizontally homogeneous atmospheric conditions and Lambertian surface, the surface spectral reflectance ρ and at-satellite spectral reflectance ρ^* of each pixel can be related by the following

equation (Vermote et al., 1997):

$$\rho^* = T_g(\rho_a + \frac{\rho_t}{1-\rho_t S} T_z T_v) \quad (3)$$

where T_g = total gases transmittance, ρ_a = intrinsic (path) radiance expressed in reflectance form, S = spherical albedo of the atmosphere, T_z = downward (sun to ground) transmittance and T_v = total upward (ground to sensor) transmittance. These parameters are simulated using the 6S code (Vermote *et al.*, 1997). The 6S code is a radiative transfer code, which is capable of simulating spaceborne or airborne remote sensing signals within the region of 0.25 and 4.0 μm assuming a cloudless atmosphere. In the 6S, the main atmospheric attenuations caused by gaseous absorption by H_2O, O_2, CO_2, and O_3, and by scattering by molecules and aerosols are taken into account.

To take into account the topographic effect, the total downward transmittance T_z is modified as:

$$T_z = \cos(i)e^{-\tau/\cos(\theta_s)} + \frac{E_d}{\cos(\theta_s)E_{sun}} \quad (4)$$

where cos(i) = cosine of solar incident angle calculated from the DEM, τ = optical depth θ_s = solar zenith angle, E_{sun} is the exoatmospheric spectral irradiances and E_d is the anisotropic diffuse solar irradiance (Richter, 1997):

To simplify the calculations, the standard atmospheric model (middle latitude winter atmospheric model) and the standard aerosol model (maritime aerosol model) provided by the 6S were used. The horizontal visibility was arbitrary set to 50 km for calculating the aerosol optical thickness at 550 nm. Furthermore, since no field measurements of the surface reflectance were available during the satellite observation ..time, the sea water was selected as the reference ground reflectance. The average at-satellite reflectance of sea water for each Landsat TM band was calculated from 10,000 pixels of sea water within the same scene. After the simulations were done, the parameters derived from simulation results were entered into Eq. 4.16 for the atmospheric and topographic corrections of the satellite image. Figure 9 shows the satellite image after the atmospheric and topographic correction. Note that certain areas in the corrected image still appear dark, which indicate that the topographic effects are not removed clearly.

A possible cause may come from the assumption of the Lambertian surface. The Lambertian assumption might not hold true under large solar incident angle condition (e.g., deep valleys located in the north-facing surfaces). Another cause might be the reflected irradiances received by the target surface that come from the adjacent terrains. For the sake of computation time, these effects are neglected in the topographic correction procedures. However, these might pose problems because vegetation have high reflectance in the reflective infrared bands.

5 Results and Discussion

5.1 Monte Carlo simulation for error propagation

The error propagation analysis was performed using the Monte Carlo method of simulation with 300 runs. The Monte Carlo method of simulation was as follows:

1. Generation of a spatially autocorrelative error field by unconditional simulation.
2. Addition of the error field to the source DEM to make a realized DEM.
3. Derivation of a map of cosine of solar

incident angle from the realized DEM.

4. Atmospheric and topographic corrections to the Landsat 5 TM data.
5. Repeating steps 1 through 4 300 times.
6. Calculation of the mean and standard deviation of each pixel for the cosine and surface reflectance map.

5.2 Magnitude of propagated DEM errors

Table 1 summarizes the global mean, standard deviations and relative errors of the cosine of solar incident angle and the spectral surface reflectance from the simulation results. The global means of the cosine map and spectral surface reflectance of the entire study site from the direct calculation (i.e., no DEM errors are taken into account) are also listed for the comparison. To distinguish the values of each pixel calculated from the step 6 of the MCM simulation described in the previous section, the terms global mean and global standard deviation were used to refer to the average value of the mean and standard deviation of the entire study site. The insignificant differences in the global means between the direct calculation and simulation results show that the DEM errors do not cause serious bias on the calculation of surface reflectance.

The global standard deviations can be regarded as the global absolute errors contributed by the DEM errors. On the other hand, the global relative error is served as the index for comparing the susceptibility of the spectral band to the DEM errors. The global relative error is defined as the ratio of the global standard deviation to the global mean.

As shown in Table 1, the global relative error of the cosine is about 7%, implying that the errors of the direct solar irradiance incident on the tilted surface is about 7%, which is contributed by the DEM errors.

The global standard deviations of the surface reflectance of band TM1 through TM3 are smaller than those of band TM4, TM5 and TM7. These might reflect the facts that the large portions of land cover within the study area are vegetations. Since the reflectance of the vegetation in reflective infrared bands is much higher than those in visible bands, the absolute error of the reflectance may follow the same behavior. The relative errors of surface reflectances of band TM1 through TM3, which belong to the visible region, are also smaller than those of band TM4, TM5 and TM7. These indicate that the reflectances in reflective infrared bands are more susceptible to DEM errors than those in visible bands. A possible reason might be that the amounts of diffuse solar irradiances incident on a tilted surface are less affected by the DEM errors. Unlike the direct solar irradiances, which come from the sun directly, the source of the diffuse solar irradiances comes from the atmosphere due to the scattering of the solar radiation by the atmosphere. Thus the change of solar incident angle of a surface caused by the DEM errors will not cause significant changes for the diffuse solar irradiances incident on the surface even the anisotropic effects are taken into account.

Besides, due to the stronger atmospheric scattering effects in visible bands than in the reflective infrared bands, the diffuse solar irradiances are more significant in visible bands. As a consequence, the reflectance in reflective infrared bands is more susceptible to DEM errors than those in visible bands.

5.3 Spatial distribution of propagated DEM errors

The maps of the standard deviation of the cosine of solar incident angle and the spectral surface reflectances for each pixel derived from MCM simulations are shown in Figure 10 through Figure 16, respectively. By mapping the standard deviation of each pixel, the spatial distribution of the propagated DEM errors and the corresponding topographic configuration could be identified.

In Figure 10, which shows the spatial distribution of the standard deviation of the cosine, the influence of the topographic effects can be identified. The sun position of the simulation is about 130 degree for the solar azimuth with 40 degree for the solar elevation and hence the north-facing surfaces tend to have larger solar incident angles while south-facing surfaces tend to have small solar incident angles. Those surfaces that face toward the sun have smaller standard deviation of cosine (i.e., higher accuracy); while those surfaces that face away from the sun tend to have larger standard deviation (i.e., lower accuracy). For the coastal areas where surfaces are relatively at, the standard deviations fall between the values for south-facing and north-facing surfaces. Such effects are caused by the facts that the fluctuations of the cosine are more rapid for large solar incident angles than those of small solar incident angles. Thus the DEM errors may have profound effects on the cosine of solar incident angle in the north-facing surfaces than in the south-facing surfaces.

As mentioned in the previous section, the accuracies of the satellite-derived reflectances are influenced by the accuracies of the direct and diffuse solar irradiances. Thus the spatial distribution of the standard deviations of the reflectance may show similarities to the spatial distribution of the standard deviation of the cosine. In Figure 11, which shows the spatial distribution of the standard deviation of the reflectance in band TM1, the value for the south-facing surfaces tend to be lower; while the north-facing ones tend to be higher and relative at coast areas fall between the south-facing and north-facing surfaces. The similar patterns can be found in the others bands. Figure 17 summarizes the relative error of spectral reflectance with the corresponding solar incident angle. The reflectance error increases with the increasing solar incident angle and has a maximum as the solar incident angle reaches 90 degree. This is not surprising because when the solar incident angle is near to 90 degree, even a small fluctuation of angle caused by DEM errors will greatly affect the cosine. As a consequence, the reflectance will have larger fluctuation for larger solar incident angle and hence more susceptible to the DEM errors.

The reflectance error drops greatly as the solar incident angle exceeds 90 degree. For the surface whose solar incident angle exceeds 90 degree, there are no direct solar irradiances incident upon it (i.e., self-shadowed) and hence less sensitive to the DEM errors.

6 Conclusion

The objective of this study is to evaluate the error propagation effects on the calculation of the cosine of solar incident angle from the digital elevation model (DEM), which is known to have certain amounts of errors expressed as root mean square error (RMSE), and its impact on the satellite derived surface reflectance. The

simulation results indicate that satellite-derived surface reflectances of the north-facing surfaces and relatively at ones are more susceptible to the DEM errors than those of the south-facing surfaces. Surface reflectances in reflective infrared bands are also more susceptible to the DEM errors than those in visible bands. In general, the contributions of the DEM errors to the relative errors of surface reflectances are smaller than 7%. However, for the north-facing surfaces, the relative may exceed 10%.

In recent years, GIS serves as a powerful tool for the environmental modelling for its varieties of analytical capabilities on geographical data. The quality of the geographical data on the results of the GIS analyses is becoming a critical issue in GIS research.

Many kinds of the geographical data stored in GIS database are generated from the remote sensing through the classified or the direct import of the images. The quality of the satellite image could affect the quality of the derivative products generated from it. This study illustrates that the errors in the satellite-derived surface reflectances are introduced by the elevation errors within the GSI 50 m DEM through the atmospheric and topographic corrections. From the perspective of error propagation, the derivative products from the surface reflectances will also potentially inherit the errors propagated from the DEM. The error propagation analysis provides a mean for tracking down the accuracy of the satellite image during the correction procedures. The analysis results come with the magnitude and the spatial distribution of the propagated errors. These information can be further incorporated into the subsequent processing for the accuracy assessment of the geographical data generated from the satellite image. Future research could be conducted to the accuracy assessment of the land cover/use classification using the atmospherically and topographically corrected satellite data that are influenced by the DEM errors.

References

Burrough, P. A., and R. A. McDonnell (1998): *Principles of Geographical Information System*, Oxford University Press, Oxford, 333 pp.

Eriksson, M. and P. P. Siska (2000): Understanding anisotropy computations, *Mathematical Geology*, 32, 683-700.

Heuvelink, G. B. M. (1998): *Error propagation in environmental modelling with GIS*, Taylor & Francis, London, 127 pp.

Horn, B. K. P. (1981): Hill shading and the reflectance map, *Proc. IEEE*, 69, 14-47.

Hunter, G. J., and M. F. Goodchild (1997): Modeling the uncertainty of slope and aspect estimated derived from spatial database, *Geographical Analysis*, 29, 35-49.

Jones, K. H. (1998): A comparison of two approaches to ranking algorithms used to compute hill slopes, *Geoinformatica*, 2, 235-256.

Murakami, H. (1995): Accuracy estimation of Digital Map series data sets published by the Geographical Survey Institute, *Geoinformatics*, 6, 59-64. (in Japanese)

Richter, R. (1997): Correction of atmospheric and topographic effects for high spatial resolution satellite imagery, *International Journal of Remote Sensing*, 18, 1099-1111.

Stein., A., F. Van der Meer, and B. Gorte (1999): *Spatial statistics for remote sensing*, Kluwer,

Dordrecht, 284 pp.

United States Geological Survey (1998): *Standards for digital elevation models*, National Mapping Program Technical Instructions, United States Department of Interior, 77 pp.

Vermote, E. F., D. Tanr´e, J. L. Deuz´e, M. Herman, and J. J. Morcrette (1997): Second simulation of the satellite signal in the solar spectrum, 6S: an overview, *IEEE Transactions on Geoscience and Remote Sensing*, 35, 675-686.

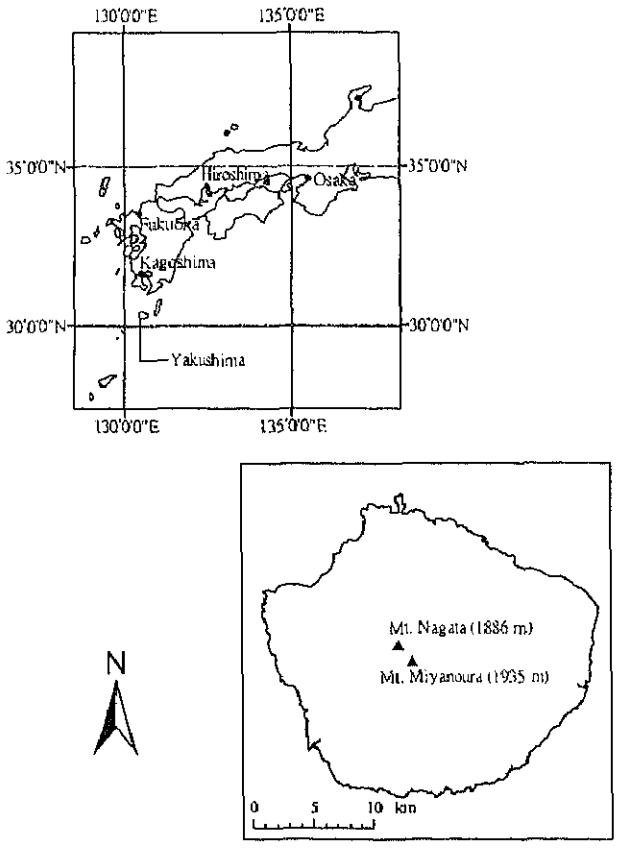

Figure 1 Location of Yakushima

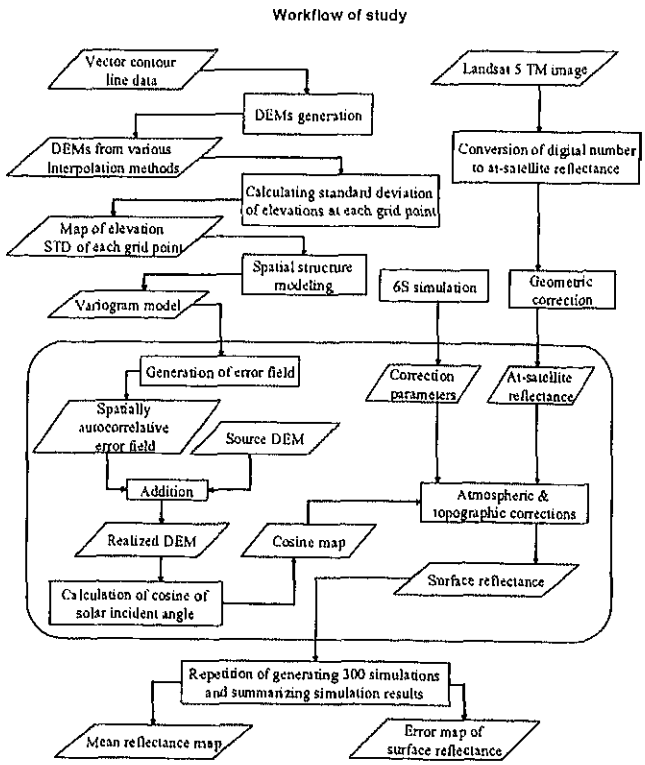

Figure 2 Work flow of analysis

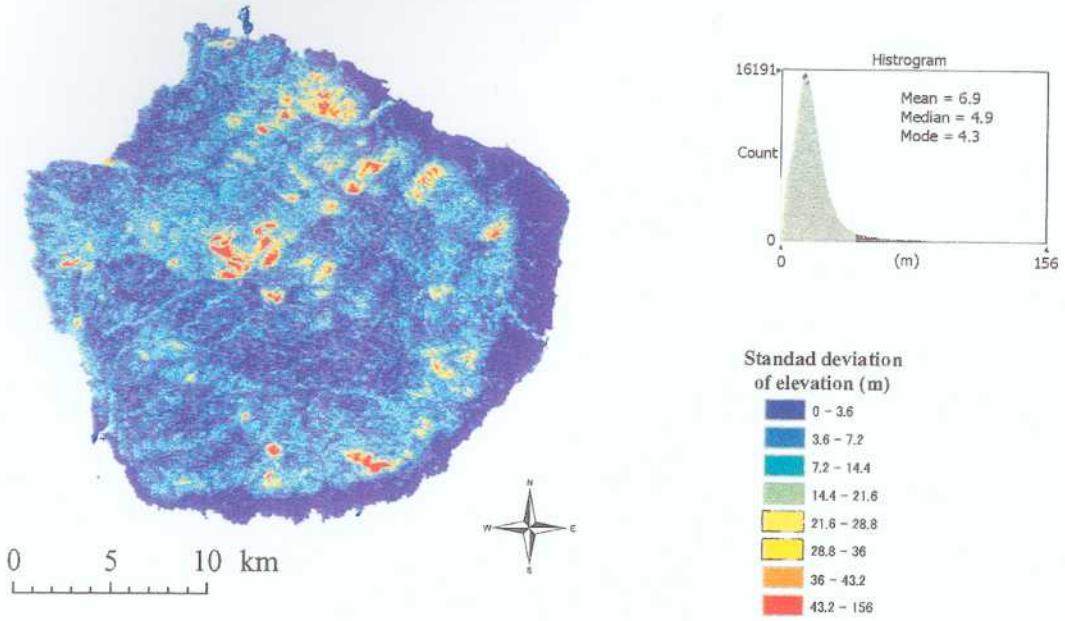

Figure 3 Standard deviation of the generated DEMs

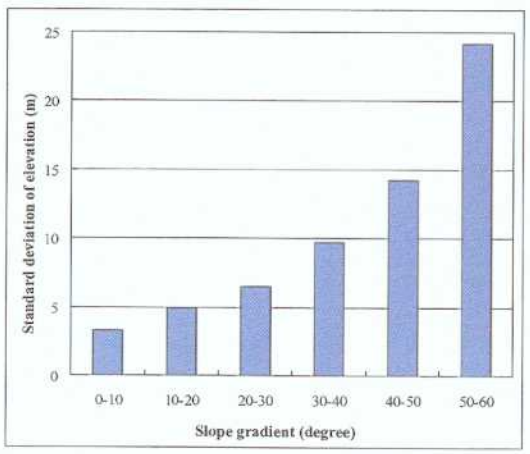

Figure 4 Magnitude of the standard deviation of generated DEMs

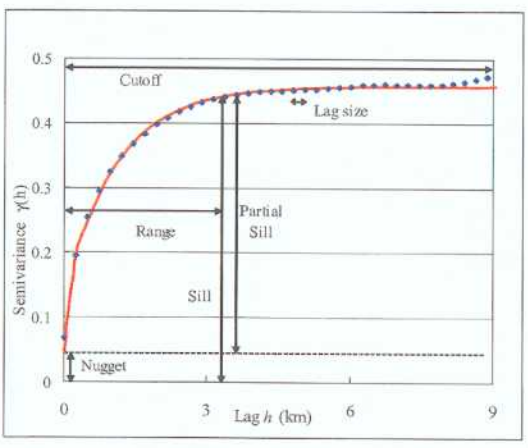

Figure 5 Experimental variogram of the standard deviation of generated DEMs

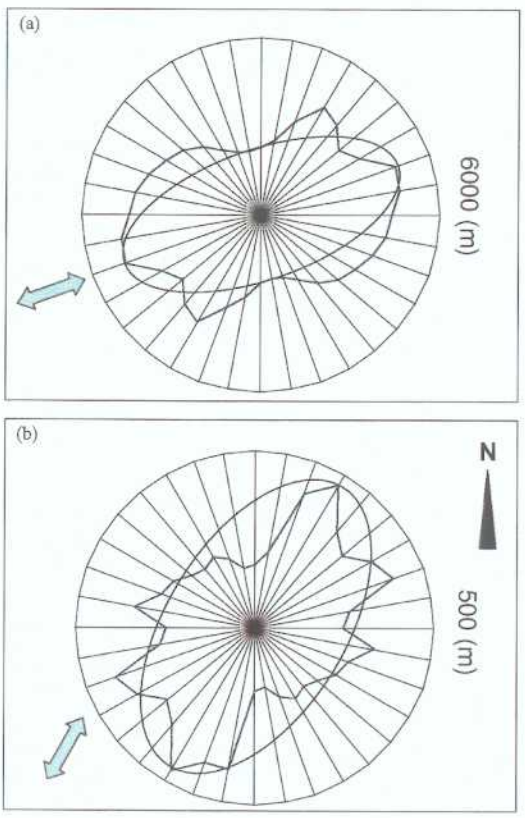

Figure 6 Variogram surface of the geometry anisotropy

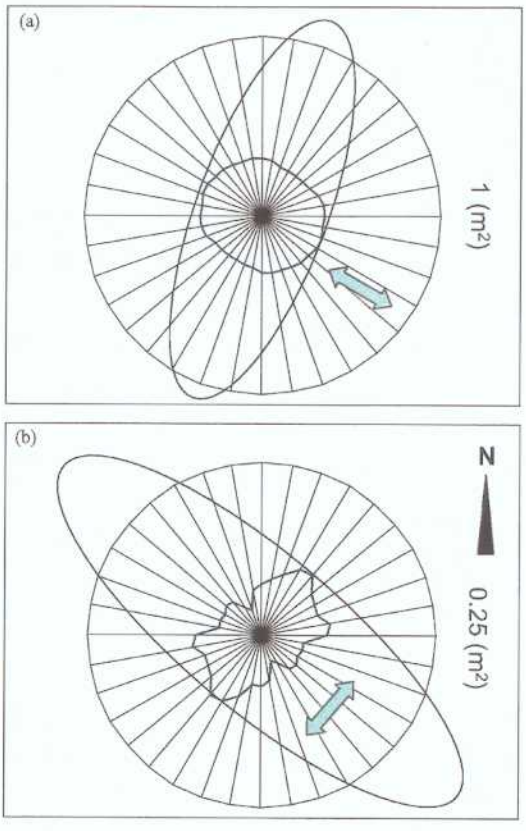

Figure 7 Variogram surface of the zonal anisotropy

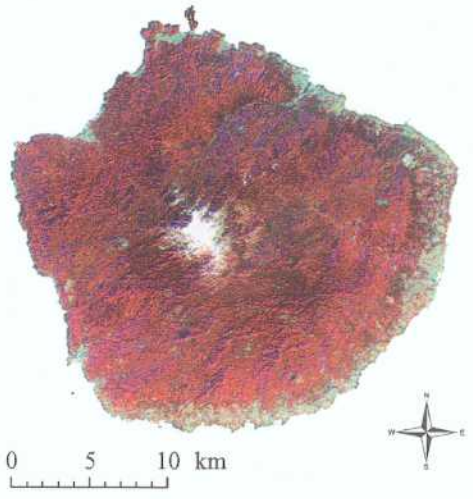

Figure 9 False color composite of Landsat 5 TM image after atmospheric and topographic corrections

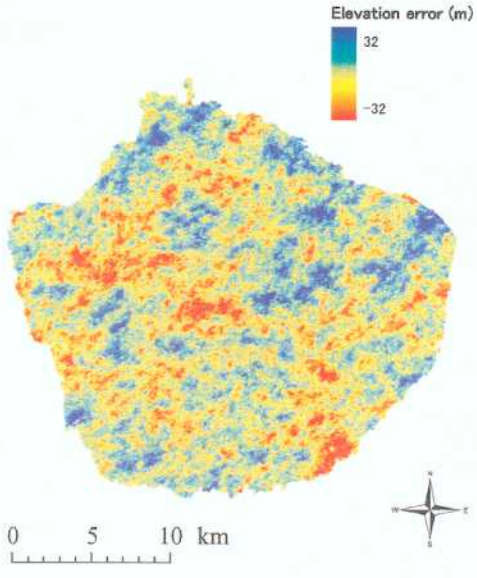

Figure 8 Single realization of the DEM's error field

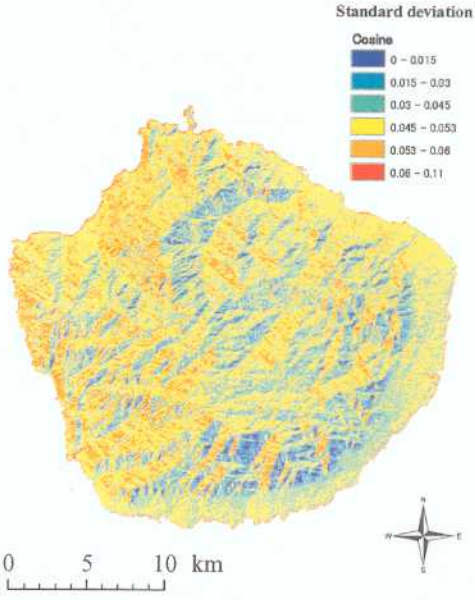

Figure 10 Standard deviation of the cosine map

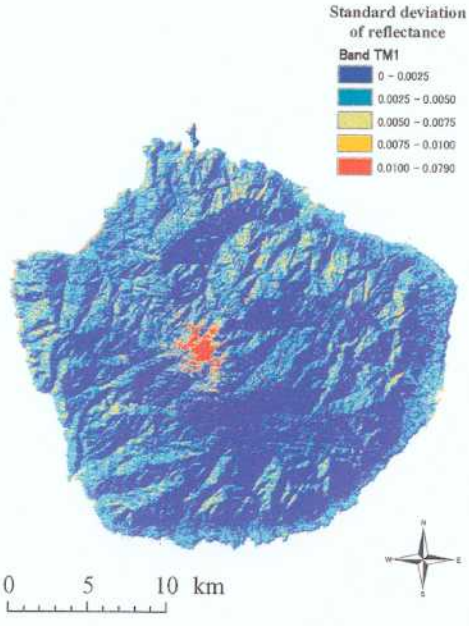

Figure 11 Standard deviation of surface reflectance of band TM1

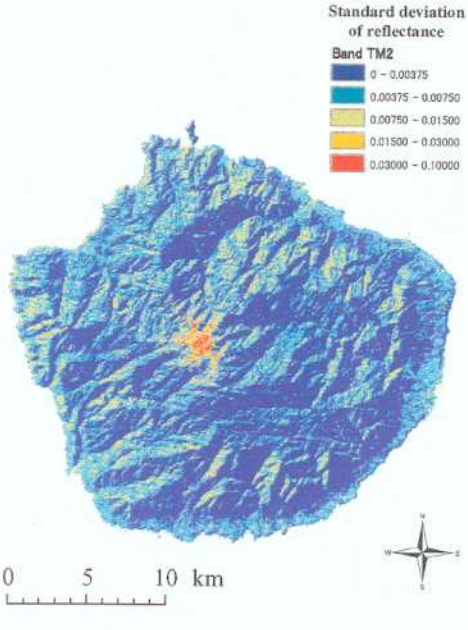

Figure 12 Standard deviation of surface reflectance of band TM2

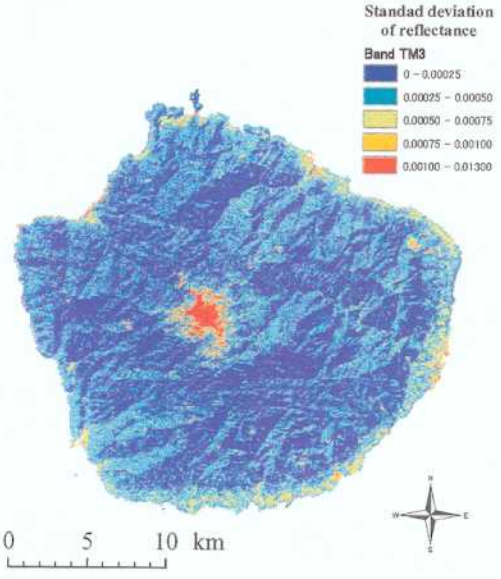

Figure 13 Standard deviation of surface reflectance of band TM3

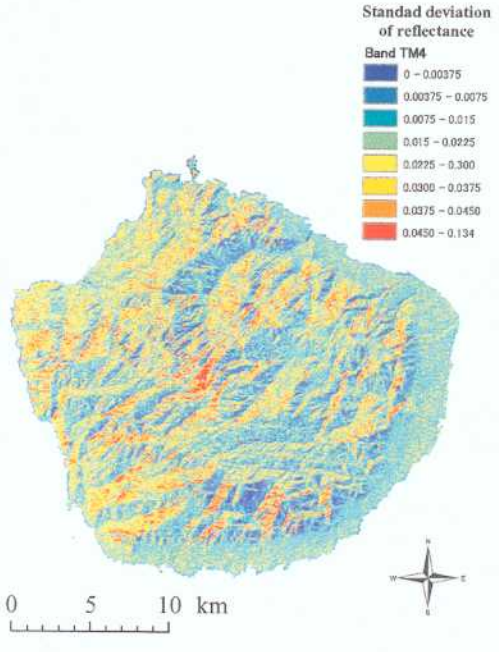

Figure 14 Standard deviation of surface reflectance of band TM4

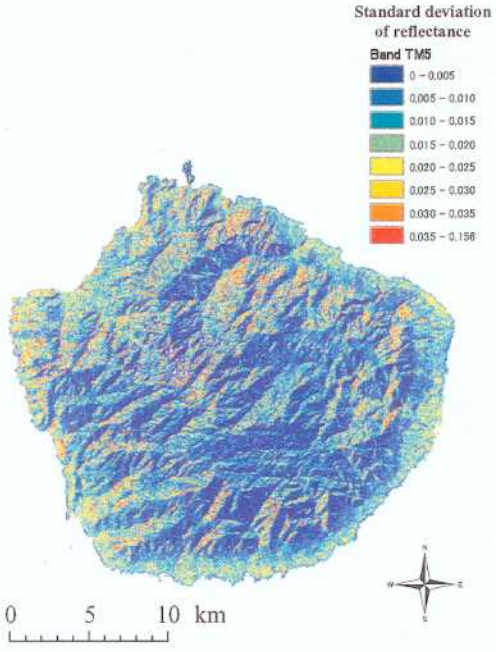

Figure 15 Standard deviation of surface reflectance of band TM5

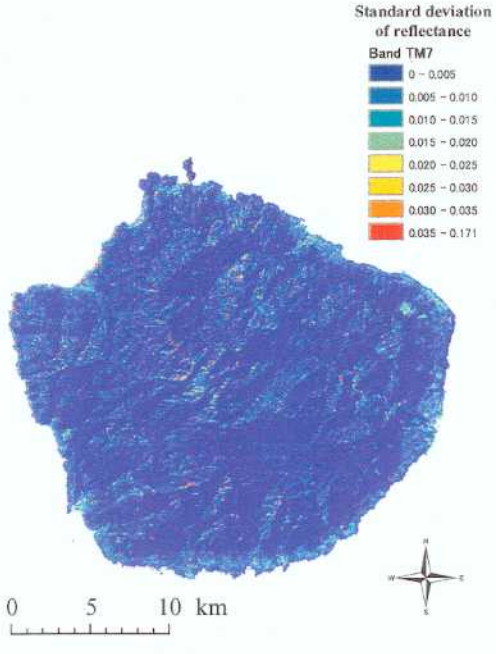

Figure 16 Standard deviation of surface reflectance of band TM7

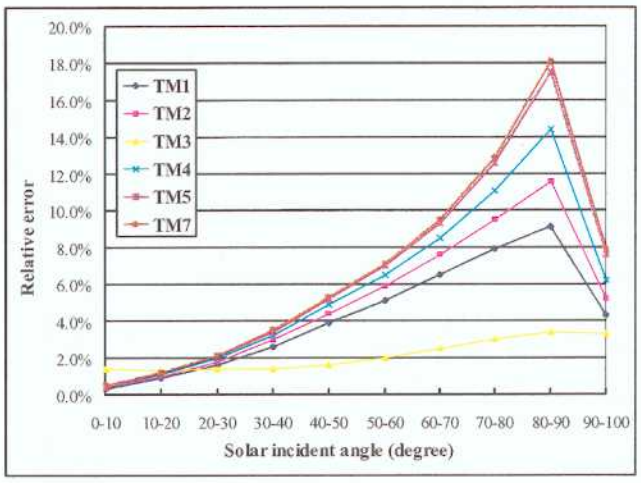

Figure 17. Magnitude of relative errors of spectral reflectance

Table 1 Summary statistics of the simulations results

	Global mean (Direct)	Global mean (Simulated)	Global STD (Simulated)	Global relative error
Cosine	0.588	0.594	0.043	0.072
TM1	0.05	0.05	0.002	0.04
TM2	0.073	0.072	0.004	0.056
TM3	0.015	0.015	0.0003	0.02
TM4	0.292	0.291	0.018	0.062
TM5	0.163	0.162	0.011	0.068
TM7	0.058	0.057	0.004	0.07